

Enhanced arsenite removal by superparamagnetic iron oxide nanoparticles *in-situ* synthesized on a commercial cube-shape sponge: adsorption-oxidation mechanism

Xiang-Yang Lou^a, Roberto Boada^{a,*}, Laura Simonelli^b, Manuel Valiente^a

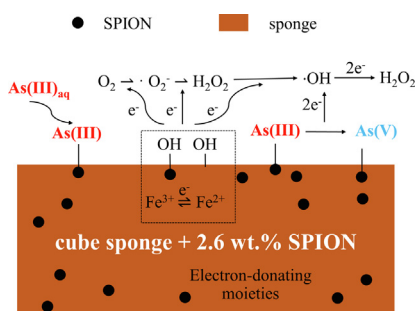
^a GTS-UAB Research Group, Department of Chemistry, Facultat de Ciències, Universitat Autònoma de Barcelona, 08193 Bellaterra, Spain

^b ALBA Synchrotron, Carrer de la Il·lum 2-26, Cerdanyola del Vallès, 08290 Barcelona, Spain

HIGHLIGHTS

- Commercial cube-shaped sponge loaded with superparamagnetic iron oxide nanoparticles (SPION) was successfully synthesized and used for As(III) removal.
- The adsorption capacity of the SPION loaded in the composite was 935.0 mg·g⁻¹ Fe with 1000 mg·L⁻¹ initial concentration, much higher than previously reported values.
- Arsenic K-edge XAS measurements revealed that As(III) was partially oxidized to less toxic As(V) upon adsorption.
- Proposed mechanism indicates that As(III) was first adsorbed on the surface of adsorbent and then oxidized by the •OH generated from Fe(III) and the –OH groups present in the adsorbent.

GRAPHICAL ABSTRACT



ARTICLE INFO

Article history:

Received 24 November 2021

Revised 17 January 2022

Accepted 18 January 2022

Available online 21 January 2022

Keywords:

Arsenite removal

Adsorption-oxidation

superparamagnetic iron oxide nanoparticles (SPION)

Commercial cube sponge

X-ray absorption spectroscopy

ABSTRACT

Hypothesis: The easy aggregation of superparamagnetic iron oxide nanoparticles (SPION) greatly reduces their adsorption performance for removing arsenic (As) from polluted water. We propose to exploit the porosity and good diffusion properties of a cube-shaped cellulose sponge for loading SPION to reduce the aggregation and to develop a composite adsorbent in the cm-scale that could be used for industrial applications.

Experiments: SPION were *in-situ* synthesized by co-precipitation using a commercial cube-shaped sponge (MetalZorb®) as support. The morphology, iron-oxide phase, adsorption performance and thermodynamic parameters of the composite adsorbent were determined to better understand the adsorption process. X-ray absorption spectroscopy (XAS) was used to investigate the chemical state of the adsorbed As (III).

Findings: The adsorption of the supported SPION outperforms the unsupported SPION (ca. 14 times higher adsorption capacity). The modelling of the adsorption isotherms and the kinetic curves indicated that chemisorption is controlling the adsorption process. The thermodynamic analysis shows that the

* Corresponding author.

E-mail address: roberto.boada@uab.cat (R. Boada).

adsorption retains the spontaneous and endothermic character of the unsupported SPION. The XAS results revealed an adsorption-oxidation mechanism in which the adsorbed As(III) was partially oxidized to less toxic As(V) by the hydroxyl free radical ($\bullet\text{OH}$) generated from Fe(III) species and by the hydroxyl groups.

© 2022 The Authors. Published by Elsevier Inc. This is an open access article under the CC BY-NC-ND license (<http://creativecommons.org/licenses/by-nc-nd/4.0/>).

1. Introduction

Arsenic (As) contamination has become a worldwide problem due to its high toxicity and carcinogenicity [1]. As is released into the environment by both natural processes and anthropogenic activities such as rock weathering, mineral extraction, wood preservation, pigments [2]. In nature waters, As is mainly found in inorganic forms, As(III) (arsenite) and As(V) (arsenate) [3]. As(III) is mostly present in underground waters whereas As(V) is mostly found in surface water [4]. Regarding the toxicity, As(III) is 60-fold more toxic than As(V) [5]. Short-term exposure to high concentrations of As can be fatal, while long-term exposure to trace concentrations of As can cause skin, lung, bladder cancers [6]. As can be transferred into the food chain through grain crops irrigated with As contaminated water and through seafood living in arsenic-containing water [7]. Exposure through contaminated drinking water is another direct pathway to humans [8]. The World Health Organization (WHO) has established a maximum concentration of As in drinking water of $10 \mu\text{g}\cdot\text{L}^{-1}$ [9]. However, still many people are exposed nowadays to high levels of As pollution in some parts of the world, particularly in developing countries [10]. Therefore, the effective removal of As from water, and in particular As(III), is markedly important for environmental protection and human health.

Among all the techniques available for As removal, adsorption is considered to be one of the most promising methods because of its advantages of being fast, easy to operate, environmentally friendly and cost-effective [11]. In recent years, magnetic iron oxide nanoparticles have attracted large attention due to their specific affinity to arsenic over other metals [12], large specific surface area [13] and easy separation from aqueous solution [14–16]. Various adsorption studies using magnetic iron oxide-based adsorbents for arsenic removal have been reported [17–20]. However, the aggregation of the nanoparticles in water negatively affects their adsorption performance [21–23]. For instance, Liu et al. [22] synthesized magnetic iron oxide nanoparticles for As removal with an average diameter of 34 nm; however, particles aggregated a lot under adsorption conditions reaching sizes over μm -size which greatly reduced the available surface area for adsorption.

To overcome this issue, materials like activated carbon [24], fly ash [25], and biomass [26] have been traditionally used as supports for nanoparticles. Although this approach helps in reducing the aggregation and provides good adsorption results, most of these composite materials reported are in powder form and, therefore, they are not suitable for direct industrial use. In addition, they are very difficult to recover when used for on-site environmental remediation applications. Indeed, when used in a fixed-bed column, the powder adsorbents tend to clog the column, and restrict the flow rate which limits their practical use. To overcome this issue, some powders have been loaded on membranes and hybrid methods combining adsorption with membrane filtration have been developed [27]. This alternative approach greatly reduces the aggregation of nanoparticulate adsorbents; however, the composite material based on membranes have a much higher cost, and it has other disadvantages such as membrane fouling that must be taken into consideration [28].

MetalZorb[®] sponge is an open-celled cellulose cube-shaped material with the properties of high porosity, high flexibility, large specific surface area and low price, which is beneficial as the support for nanoparticles. This material is claimed to contain free available iminodiacetate groups to interact with superparamagnetic iron oxide nanoparticles (SPION) by chelation. In this work, we propose this commercial cube-shaped MetalZorb[®] sponge to support SPION as a composite material for the removal of As(III) from aqueous solutions. The adsorption performance of this composite material was studied and compared with the unsupported SPION in powder form. Furthermore, our X-ray absorption spectroscopy study at different depths of the cube adsorbent has allowed us to investigate the adsorption mechanisms at molecular scale and the redox processes that may take place upon adsorption.

2. Materials and methods

2.1. Materials

All reagents used were of analytical grade. Iron chloride hexahydrate ($\text{FeCl}_3\cdot 6\text{H}_2\text{O}$) and ferrous chloride tetrahydrate ($\text{FeCl}_2\cdot 4\text{H}_2\text{O}$) were used in the synthesis of SPION and sponge-loaded SPION. Sodium arsenite (NaAsO_2) was used as the source of As(III). A $1000 \text{ mg}\cdot\text{L}^{-1}$ As(III) stock solution was initially prepared, and then diluted to the required concentration. Hydrogen chloride (HCl) and sodium hydroxide (NaOH) were used to adjust the pH during adsorption experiments.

Commercial cube-shaped MetalZorb[®] adsorbent was kindly supplied by CleanWay Environmental Partners, Inc. (Portland, USA). The material is an open-celled cellulose sponge (hereafter referred simply as “sponge”) as described in our previous publications [29]. The averaged dimensions of the cube are (length \times width \times height): $12.8 \pm 1.8 \times 10.1 \pm 1.1 \times 7.3 \pm 1.3 \text{ m}$. Each cube has an average weight of $0.20 \pm 0.02 \text{ g}$.

2.2. Synthesis of the adsorbents and characterization

SPION were synthesized by the co-precipitation method [30]. In the synthesis of sponge-loaded SPION, raw sponge was pre-treated and deprotonated following the suggestion from the manufacturer and afterwards the nanoparticles were synthesized *in-situ*. Details about the synthesis methods for SPION and sponge-loaded SPION can be found in section S1 of the Support information (SI). Regarding the synthesis mechanisms, the iminodiacetate groups present on the surface of the sponge act as anchor points for the nanoparticles by chelation at the onset of the nucleation stage.

The surface area data of unsupported SPION calculated from N_2 adsorption analysis is $92.3 \text{ m}^2\cdot\text{g}^{-1}$. Cube adsorbents were split into three regions (surface, quarter, and center) to get information at different depths, as shown in Fig. S1. The SEM and TEM images confirmed the successful loading of SPION on the porous structures of the sponge (see top panel of Fig. S2). The average nanoparticle size calculated by Image-pro plus software (Media Cybernetics, Silver Spring, USA) from the TEM images were 12.7 and 13.8 nm for surface and center parts, respectively (see middle and bottom panels of Fig. S2). Hence, the size of the SPION loaded on the sponge

has been greatly reduced respect to the effective particle size of the aggregated unsupported SPION (~100 nm). Unfortunately, some degree of aggregation is still present in the composite. The slightly different particle size of the SPION at surface and center parts might be due to the slightly reduction of the diffusion in the inner part of the cube respect to the surface part which may promote a rapid growth of the particles. X-ray absorption near edge structure (XANES) spectra of Fe K-edge collected on SPION, sponge-loaded SPION (surface), sponge-loaded SPION (center), indicated that the iron oxide phase was maghemite ($\gamma\text{-Fe}_2\text{O}_3$) (see Fig. S3). In addition, the XANES comparison of old and fresh composite material showed that iron oxidation state was stable over time (see Fig. S4). The loading amount of the SPION was around 2.6 wt% in the composite as determined by ICP-MS analysis.

2.3. Adsorption experiments

Adsorption experiments were performed by putting 0.20 g adsorbent (either SPION, cube sponge or cube sponge-loaded SPION) in contact with 25.0 ml of As(III) solution. The tubes were agitated mechanically at 300 rpm using a rotary shaker. Adsorption experiments were performed at different temperatures by putting the shaker inside of an incubator. Adsorption experiments with different initial concentrations were performed for concentrations within the range 10–1000 $\text{mg}\cdot\text{L}^{-1}$ As(III) at pH 7.0 shaking during 120 min; experiments at different contact times (1–480 min) were performed at pH 7.0 and using a 200 $\text{mg}\cdot\text{L}^{-1}$ initial concentration; experiments at different pH values were performed by adjusting the pH from 3.0 to 10.0 with 200 $\text{mg}\cdot\text{L}^{-1}$ initial concentration and agitating during 120 mins.

After adsorption, for SPION, the nanoparticles were magnetically separated. In the case of sponge or sponge-loaded SPION, the adsorbent was separated by decanting the aqueous solution. The amount of As(III) adsorbed was determined as the difference of the remaining As(III) in the solution from the initial one. The As(III) concentration was determined by applying the molybdenum blue spectrophotometric method after oxidating the As(III) to As(V) with potassium permanganate (KMnO_4) (further details can be found in section S4 in SI). The adsorption capacity at equilibrium was calculated using the following equation:

$$q_e = (C_0 - C_e) \frac{V}{m} \quad (1)$$

where q_e ($\text{mg}\cdot\text{g}^{-1}$) is the adsorption capacity, V (L) is the volume of the arsenic solution, m (g) is the dry weight of the adsorbent, C_0 and C_e ($\text{mg}\cdot\text{L}^{-1}$) are initial and equilibrium concentrations of As(III) solution, respectively.

2.4. Isotherm and kinetic modeling

To further understand the As(III) adsorption behavior, experimental adsorption isotherms were fitted with Langmuir, Freundlich and Temkin isotherm models. Separately, the adsorption data collected at different contact times were fitted to pseudo-first order and pseudo-second order kinetic models. Detailed information about these isotherm and kinetic models can be found in section S5 of the SI.

2.5. Synchrotron radiation based XAS analysis

X-ray absorption spectroscopy (XAS) technique was used to study the oxidation state of As after adsorbed on the different adsorbents (SPION, sponge and sponge-loaded SPION). An initial concentration of 200 $\text{mg}\cdot\text{L}^{-1}$ As(III) and a contact time of 120 min were used. The effect of the adsorption temperature was also studied by performing adsorption experiments at 293 and 343 K. After

decanting the aqueous solution, the solid was washed three times with Milli-Q water, afterwards, the adsorbents were dried in an oven at 50 °C for 24 h. Arsenic trioxide, As(III), and arsenic pentoxide, As(V), were used as reference materials. All samples and references were milled and pressed into pellets for performing the measurements.

The XAS experiment at the As K-edge was carried out at BL22 CLÆSS beamline of ALBA CELLS synchrotron using a Si(3 1 1) double crystal monochromator [31]. Measurements of sponge and SPION samples were performed in fluorescence mode using a multi-element silicon drift detector, while measurements for sponge-loaded SPION and As references were collected in transmission mode using ionization chambers. To reduce the self-absorption effect, SPION powder was homogeneously mixed with cellulose using a SPION:cellulose ratio of 1:10. Special care was taken when setting up the fluorescence measurements to minimize the damping effect due to the dead-time. The measurements were carried out at liquid nitrogen temperature to minimize any possible radiation damage. XAS data analysis was performed according to standard procedures using ATHENA software of the Demeter package [32].

3. Result and discussion

3.1. Adsorption performance

Batch experiments were performed to study the adsorption behavior of the materials. Different parameters (initial concentration, contact time, and pH) that affect As(III) adsorption were investigated. The adsorption capacities of the unsupported SPION, sponge-loaded SPION (composite material) and SPION in composite (considering only the mass of the loaded SPION in the composite) were compared. As seen in (Fig. 1a), the adsorption capacity of SPION and sponge-loaded SPION increased with As(III) initial concentration. In contrast, the adsorption of As(III) in sponge was below the detection limit of the colorimetric method used and therefore it can be considered negligible. This means that the sponge acts mainly as a support for reducing the aggregation of SPION. Our results show that the sponge-loaded SPION composite has less adsorption capacity than the unsupported SPION, however, when considering only the small mass fraction of SPION in the composite, 2.6 wt%, there is an enhancement of the adsorption capacity over one order of magnitude respect to the unsupported SPION. For instance, at the maximum initial concentration used (1000 $\text{mg}\cdot\text{L}^{-1}$), the adsorption capacity of the composite per gram of SPION is 655.0 $\text{mg}\cdot\text{g}^{-1}$ for the composite and only 45.3 $\text{mg}\cdot\text{g}^{-1}$ for the unsupported SPION. In other words, the SPION loaded in the sponge displays ca. 14 times the adsorption capacity of the unsupported SPION. This difference is due to the greatly reduced aggregation of the nanoparticles when loading the SPION on the sponge as can be seen in the TEM images (Fig. S2).

The dependence of adsorption capacity respect to the contact time is shown in (Fig. 1b). There is a sharp increase in the adsorption capacity during the initial 60 min. This can be attributed to the large number of adsorption sites initially available on the surface of the adsorbent. When normalizing by the mass fraction of the loaded SPION, the adsorption capacity of SPION in the composite material reaches 295.6 $\text{mg}\cdot\text{g}^{-1}$. This is ca. 14 times higher than the one of the unsupported SPION (21.0 $\text{mg}\cdot\text{g}^{-1}$).

The adsorption behavior at equilibrium did not show a significant dependence with the pH between 3.0 and 10.0, see Fig. S5. This is due to the fact that uncharged H_3AsO_3 ($\text{p}K_a = 9.2$) is the main As(III) species. Therefore, As(III) cannot be adsorbed by electrostatic interaction [33,34].

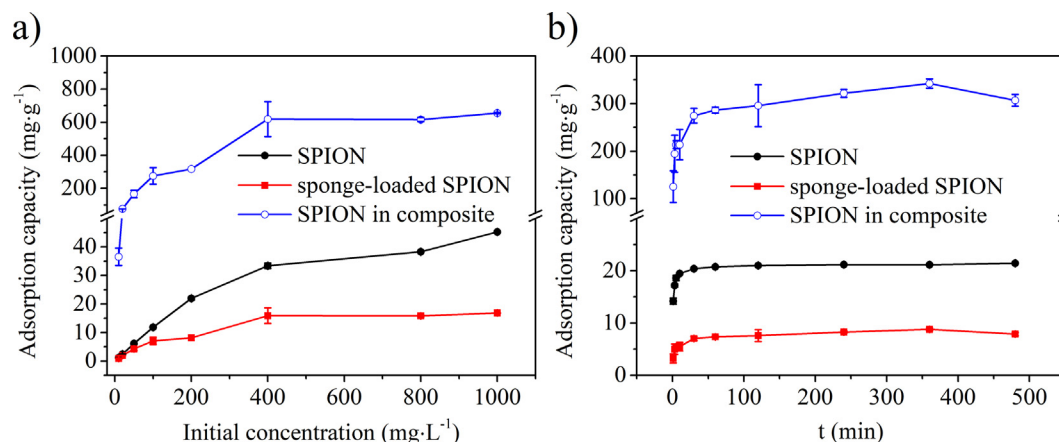


Fig. 1. As(III) adsorption capacity of SPION, sponge-loaded SPION and SPION in composite: initial concentration (a) and contact time (b).

3.2. Adsorption isotherm modeling

The results for the As(III) adsorption isotherm modeling for SPION, sponge-loaded SPION and SPION in composite are shown in Fig. 2 and Table S1. Langmuir, Freundlich and Temkin isotherm models were used. Relatively good fits ($R^2 > 0.90$) were found for the three models for all the adsorbents. For unsupported SPION, the best fit was found for the Temkin model (Temkin > Langmuir > Freundlich). For the composite material and for the supported SPION, the Langmuir model has a higher correlation coefficient than the Temkin model (Langmuir > Temkin > Freundlich), however, the heterogeneity of the composite adsorbent should be taken into consideration and therefore the Langmuir model is not suitable for these adsorbents since it considers single layer and homogeneous adsorption. Hence, considering both the fitting results and the characteristics of the materials, the Temkin model provides the best agreement for all adsorbents. This model explicitly considers the adsorbent–adsorbate interactions [35]. As can be seen from the fitting results (Fig. S1), the values of b_T (related to the heat of adsorption) for unsupported SPION, sponge-loaded SPION and SPION in composite are all positive, which implies that in all the cases the adsorption is exothermic. In addition, the A_T (related to the binding energy) value of unsupported SPION is substantially larger than that of the composite material, which means a stronger interaction

between the SPION–As(III) ion surface than sponge–As(III) surface. This result is consistent with our adsorption experiment data showing that the sponge does not adsorb As(III).

3.3. Kinetics

Kinetic parameters were determined to assess the efficiency and the mechanism of the adsorption process [36,37]. The fitting results using the pseudo-first order kinetic model and pseudo-second order kinetic model are displayed in Fig. 3 and Table S2. The results show that the As(III) adsorption process on the adsorbents is best interpreted by the pseudo-second order kinetic model. This indicates that chemisorption is driving the adsorption process rate, which is in line with the results obtained from the isotherm modelling.

3.4. Thermodynamic determinations

Thermodynamic parameters such as Gibbs free energy change (ΔG°), enthalpy change (ΔH°) and entropy change (ΔS°) were determined to predict the feasibility and thermodynamic nature of the adsorption process [38,39]. The calculated method is displayed in section S7 and the thermodynamic parameters determined are displayed in Table 1.

The adsorption of As(III) on the composite adsorbent has negative ΔG° , positive ΔH° and positive ΔS° as SPION. The negative ΔG° values indicate that the adsorption of As(III) onto SPION is spontaneous. The values of ΔH° for SPION and sponge-loaded SPION are 10.50 and 4.68 kJ·mol⁻¹, respectively, which indicates that the As (III) adsorption on both adsorbents is an endothermic process. The positive ΔS° likely resulted from the release of orderly structured hydration water and subsequent increase in randomness with increased concentration of adsorbed As(III) on the solid surface [40,41].

3.5. Compare of the adsorption capacity with similar adsorbent system

Considering the Fe content in the adsorbents, the equilibrium adsorption capacities of unsupported SPION and supported SPION at 1000 mg·L⁻¹ As(III) initial concentration are 64.7 and 935.0 mg·g⁻¹ Fe, respectively. This indicates that the loading of SPION on the sponge can significantly improve the adsorption capacity respect to the unsupported SPION. This can be attributed to the less aggregation of the SPION when loaded in the sponge support which increases the effective surface available for the adsorption process.

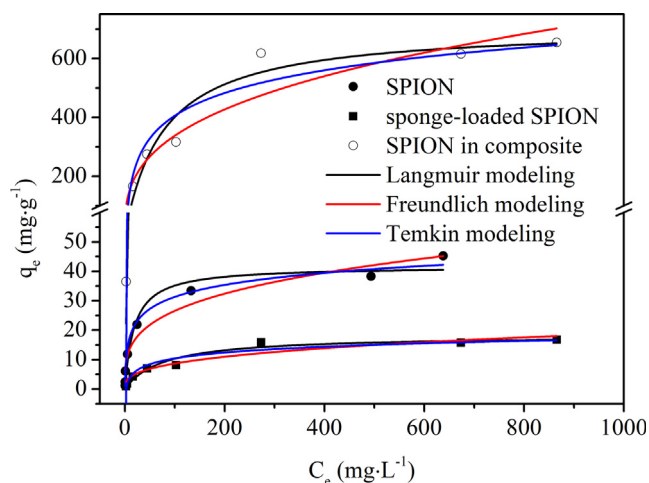


Fig. 2. As(III) adsorption isotherm modeling for SPION, sponge-loaded SPION and SPION in composite at 293 K.

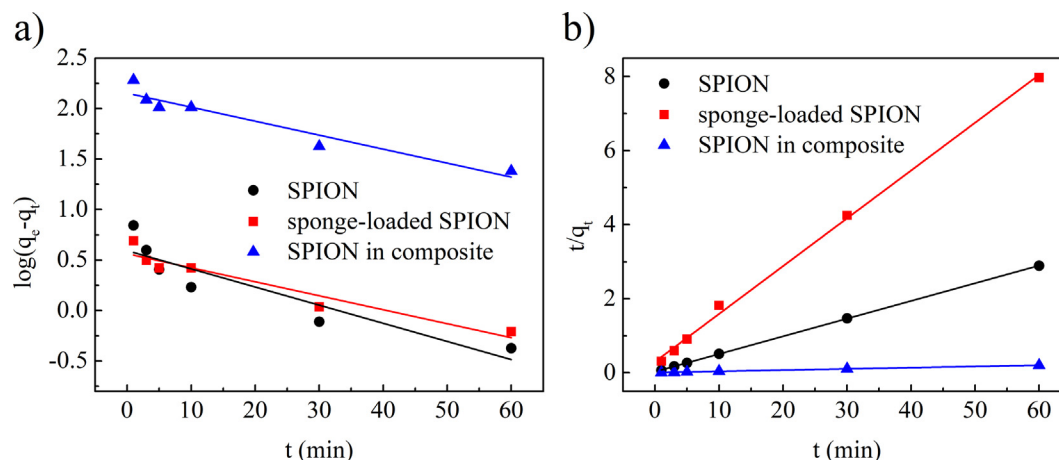


Fig. 3. Kinetic modeling for As(III) adsorption on SPION, sponge-loaded SPION and SPION in composite: Pseudo-first order model (a) and Pseudo-second order model (b).

Table 1

Thermodynamic parameters for As(III) adsorption on SPION, sponge-loaded SPION and SPION in composite.

Adsorbent	Temperature(K)	ΔG° (kJ·mol ⁻¹)	ΔH° (kJ·mol ⁻¹)	ΔS° (J·mol ⁻¹ ·K ⁻¹)
SPION	293	-16.43	10.50	91.88
	318	-18.73		
	343	-21.03		
Sponge-loaded SPION	293	-10.68	4.68	52.39
	318	-11.99		
	343	-13.30		
SPION in composite	293	-19.60	4.68	82.82
	318	-21.67		
	343	-23.74		

In addition, the adsorption capacities of both unsupported SPION and supported SPION are compared with their similar system reported adsorbents, the results are listed in Table 2. In our case, we are not quoting the maximum adsorption capacity extrapolated from the isotherm modelling but the adsorption capacity for an initial As(III) concentration of 1000 mg·L⁻¹, and this value would be lower than the hypothetical maximum adsorption capacity. We can clearly see, the adsorption capacity of unsupported SPION is significantly higher when compared with both the adsorption capacities of commercial GEH-102 [42] and laboratory synthesized magnetite nanoparticles by Liu et al. [22]. A significant improvement in adsorption capacity of SPION supported by cube sponge was also found when compared with other reported Fe-based composite powder adsorbents [43–46]. Besides, one of the additional advantages of our cube sponge-based composite is that, once exhausted, it can be easily compressed into a very small volume, thus facilitating its transport and waste disposal.

3.6. As K-edge XAS measurements

Due to the different toxic risks associated with the As species [47], it is important to understand the fate of adsorbed As(III) and to discern any possible redox processes that may take place upon adsorption. Indeed, the oxidation state and the speciation of As determine its toxicity and mobility in the environment [48]. In that respect, X-ray absorption near-edge structure (XANES) experiments were performed to investigate the coordination environment and the chemical state of As(III) adsorbed on SPION, sponge and sponge-loaded SPION. The influence of the different temperatures and the different depths of cube adsorbents (C, Q, S) were also studied. (Fig. 4a) shows the comparison of the As K-edge XANES spectra of the adsorbent materials with the reference compounds for As(III), arsenic trioxide, and As(V), arsenic pentoxide. The As reference compounds display a markedly different spectral profile. The pentoxide is shifted ~ 3.7 eV towards high

Table 2

Comparison of the As(III) adsorption capacities of unsupported SPION and SPION in composite with similar Fe-based systems.

Support	Size	Fe content (wt%)	Iron phase	q_e (mg·g ⁻¹ Fe)	Reference
None	12.0 nm	70.0	γ -Fe ₂ O ₃	64.7 *	This work
Cube sponge	13×10×7 mm	1.8	γ -Fe ₂ O ₃	935.0 *	This work
None	34 nm	72.4	Fe ₃ O ₄	23.0	[22]
None	0.3–2 mm	52–62	Fe(OH) ₃ and	33.3	[42]
			β -FeO(OH)		
Cork	0.8–2 mm	2.4	iron (oxy)hydroxides	204.2	[43]
Cellulose	0.02 mm	36	Fe ₂ O ₃	64.3	[44]
Alginate beads	0.5 mm	30	2-line ferrihydrite	159.3	[45]
Polyurethane foam	6 nm	19.3	Fe ₃ O ₄	178.7	[46]

(*) at 1000 mg·L⁻¹.

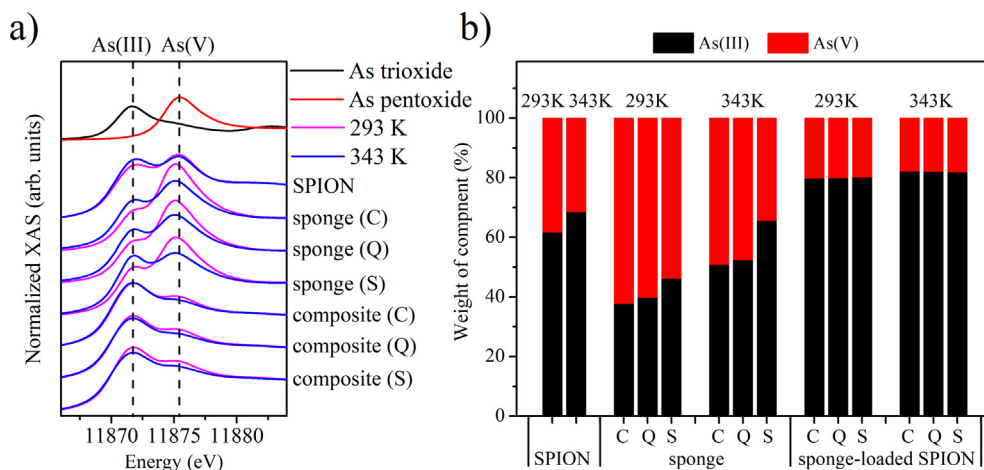


Fig. 4. As K-edge XAS spectra of adsorbents after adsorbing As(III) at different temperatures (a) and corresponding peak fitting results (b). Arsenic trioxide and pentoxide compounds are also included for comparison and used for peak fitting references.

energy with respect to the trioxide. In addition, the white-line feature (first resonance after the absorption rising edge) appears at 11875.5 and 11871.7 eV for pentoxide and trioxide, respectively. By direct comparison of the position of the absorption edge and the white-line, we found that some of the As(III) was oxidized to As(V) upon adsorption. This oxidation was related to the existence of the reactive oxygen species (ROS), especially hydroxyl free radical ($\bullet\text{OH}$) and hydrogen peroxide (H_2O_2) generated by Fe(III) [22,49] and the hydroxyl groups ($-\text{OH}$) [50] present in SPION and sponge adsorbents.

Furthermore, no As(V) ions were found in the aqueous solution before and after adsorption, implying that this oxidation reaction mainly occurred on the surface of the adsorbent. Thus, a combination of adsorption-oxidation mechanisms is proposed. Under neutral and aerobic conditions, As(III) is firstly adsorbed on the surface of the adsorbents, and then oxidized by the generated ROS from the composite material. The proposed mechanism is shown in Fig. 5.

In addition, to unravel the two As species, a peak fitting analysis of the XANES spectra was performed (see details in section S8). The results are displayed in (Fig. 4b) and Table S5. When comparing the different adsorbents it was found that the largest amount of As(III) oxidized to As(V) was taking place in sponge, 30–60%. This can be due to the large density of functional sites that can oxidize As(III)

respect to negligible As(III) adsorbed on the sponge. On the other hand, SPION showed a larger amount of As(V) than sponge-loaded SPION. This can be related to the low loading of the $\gamma\text{-Fe}_2\text{O}_3$ nanoparticles in the composite material (2.6 wt%). In other words, the As:Fe ratio in the composite is much larger than in the unsupported SPION, which turns into less available Fe(III) species to contribute to the As(III) oxidation process after adsorption. In all the materials, the oxidation of As(III) to As(V) was more favorable at lower temperatures since the decomposition of H_2O_2 at higher temperatures results in a decrease of $\bullet\text{OH}$ [51]. However, the difference in the oxidation of sponge-loaded SPION caused by the temperature was very small (only $\sim 2\%$). This can be related with the small mass loading of SPION in the composite as mentioned above. After adsorption, the amount of $-\text{OH}$ functional site available in the loaded SPION is much lower than in the case of unsupported SPION.

When comparing different depths of the cube adsorbents, for sponge, the As(III) adsorbed in center part showed a higher amount of As(V) species due to the diffusion constraints that increase towards the center of the cube, hence, reducing the recirculation of hydroxyl free radicals and favoring the interaction. However, for sponge-loaded SPION, the As(III) oxidation reaction is controlled by the mass of SPION, which is rather constant in the whole cube and yields similar As(V) conversion in all parts of the cube. In addition, it is important to bear in mind that the amount of As adsorbed in sponge is almost negligible and, therefore, neither the effects of the temperature nor the penetration depth will be significantly reflected in the oxidation process taking place in the cube composite adsorbent.

4. Conclusions

In contrast to the broadly reported iron-based composite adsorbents in powder form [52–54], here we have reported the synthesis, characterization and molecular adsorption mechanism for a cm-scale cube-shaped composite adsorbent. This adsorbent material is composed by superparamagnetic iron oxide nanoparticles (SPION) *in-situ* co-precipitated in a commercial open-cellulose sponge. Our results show that the nanoparticle aggregation is greatly reduced in the composite which yields a much better As(III) adsorption performance than in the case of the unsupported SPION. Hence, the composite material retains the advantageous properties of SPION for As adsorption. Moreover, the results from our XAS study indicate that, once adsorbed, the highly toxic and

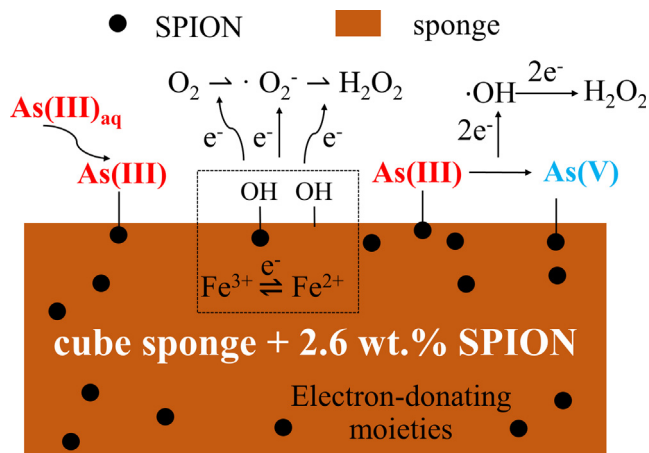


Fig. 5. Proposed mechanism of the As(III) adsorption-oxidation process taking place on the surface of the composite adsorbent.

carcinogenic As(III) is partially oxidized to less toxic As(V), which is desirable for the treatment of As(III)-contaminated waters. Researchers using unsupported nanoparticles or composite powders have reported similar results [22,55], however, our study has also revealed that this As(III) oxidation is not temperature-dependent. In addition, a similar oxidation state of the adsorbed As was found at different cube depths which demonstrates that the same adsorption process occurs at the different parts of the cube composite. This is due to the good diffusion properties of the sponge material and the rather homogeneity of the SPION loaded in the porous sponge. The adsorption-oxidation mechanism proposed in this study includes a first adsorption of As(III) on the surface of the adsorbent, and its oxidation afterwards to As(V) by the $\bullet\text{OH}$ radicals generated from Fe(III) and the $-\text{OH}$ groups present in SPION and sponge adsorbents under neutral conditions. In brief, this cube sponge-loaded SPION offers high affinity and good adsorption capacity for As(III) together with good diffusion properties and favourable cube-shape which are desirable for industrial applications.

CRediT authorship contribution statement

Xiang-Yang Lou: Methodology, Formal analysis, Writing – original draft, Writing – review & editing. **Roberto Boada:** Conceptualization, Formal analysis, Writing – original draft, Writing – review & editing. **Laura Simonelli:** Methodology. **Manuel Valiente:** Conceptualization, Methodology, Supervision, Writing – review & editing, Funding acquisition.

Declaration of Competing Interest

The authors declare that they have no known competing financial interests or personal relationships that could have appeared to influence the work reported in this paper.

Acknowledgements

We acknowledge CleanWay Environmental Partners, Inc. for kindly supplying the cube-shaped MetalZorb[®] sponge. We acknowledge ALBA synchrotron facility for beamtime no. 2018093125 at BL22-CLAESS beamline. This research was financially supported by the project CTM2015-65414-C2-1-R from MINECO ministry of Spain. X-Y. Lou acknowledges the China Scholarship Council for his PhD fellowship (No. 201708110179). R. Boada acknowledges funding support from the European Union's Horizon 2020 research and innovation program under the Marie Skłodowska-Curie grant agreement No. 665919.

Appendix A. Supplementary material

Supplementary data to this article can be found online at <https://doi.org/10.1016/j.jcis.2022.01.119>.

References

- [1] G.A. Borges, G.M.D. Ferreira, K.P.F. Siqueira, A. Dias, K.O.N. Navarro, S.J.B.e. Silva, G.D. Rodrigues, A.B. Mageste, Adsorption of organic and inorganic arsenic from aqueous solutions using MgAl-LDH with incorporated nitroprusside, *J. Colloid Interface Sci.* 575 (2020) 194–205, <https://doi.org/10.1016/j.jcis.2020.04.078>.
- [2] V. Reis, A.C. Duarte, Occurrence, distribution, and significance of arsenic speciation, in: *Compr. Anal. Chem.*, Elsevier, 2019: pp. 1–14. <https://doi.org/10.1016/bs.coac.2019.03.006>.
- [3] Z. Yin, J. Lützenkirchen, N. Finck, N. Celaries, K. Dardenne, H.C.B. Hansen, Adsorption of arsenic(V) onto single sheet iron oxide: X-ray absorption fine structure and surface complexation, *J. Colloid Interface Sci.* 554 (2019) 433–443, <https://doi.org/10.1016/j.jcis.2019.07.024>.
- [4] M.R. Akanda, I.-S. Kim, D. Ahn, H.-J. Tae, W. Tian, H.-H. Nam, B.-K. Choo, B.-Y. Park, In Vivo and In Vitro Hepatoprotective Effects of Geranium koreanum Methanolic Extract via Downregulation of MAPK/Caspase-3 Pathway, *Evidence-Based Complement. Altern. Med.* 2017 (2017) 1–12, <https://doi.org/10.1155/2017/8137627>.
- [5] N.S. Ferreira, L.H.B. Oliveira, V. Agrelli, A.F. de Oliveira, A.R.A. Nogueira, A. Oliveira, M.H. Gonzalez, Bioaccumulation and acute toxicity of As(III) and As(V) in Nile tilapia (*Oreochromis niloticus*), *Chemosphere* 217 (2019) 349–354, <https://doi.org/10.1016/j.chemosphere.2018.11.013>.
- [6] A. Mehri, Trace elements in human nutrition (II) - An update, *Int. J. Prev. Med.* 11 (2020) 2, https://doi.org/10.4103/ijpvm.IJPVM_48_19.
- [7] K. Karimyan, M. Alimohammadi, A. Maleki, M. Yunesian, R.N. Nodehi, A.R. Foroushani, The mobility of arsenic from highly polluted farmlands to wheat: Soil-Plant transfer model and health risk assessment, *L. Degrad. Dev.* 31 (12) (2020) 1560–1572, <https://doi.org/10.1002/ldr.3552>.
- [8] N.I. Khan, G. Owens, D. Bruce, R. Naidu, Human arsenic exposure and risk assessment at the landscape level: a review, *Environ. Geochem. Health.* 31 (S1) (2009) 143–166, <https://doi.org/10.1007/s10653-008-9240-3>.
- [9] E. Shaji, M. Santosh, K.V. Sarath, P. Prakash, V. Deepchand, B.V. Divya, Arsenic contamination of groundwater: a global synopsis with focus on the Indian Peninsula, *Geosci. Front.* 12 (3) (2021) 101079, <https://doi.org/10.1016/j.gsf.2020.08.015>.
- [10] R. Arora, Nano adsorbents for removing the arsenic from waste/ground water for energy and environment management - a review, *Mater. Today Proc.* 45 (2021) 4437–4440, <https://doi.org/10.1016/j.matpr.2020.12.546>.
- [11] H. Zeng, L. Zhai, T. Qiao, Y. Yu, J. Zhang, D. Li, Efficient removal of As(V) from aqueous media by magnetic nanoparticles prepared with Iron-containing water treatment residuals, *Sci. Rep.* 10 (2020) 9335, <https://doi.org/10.1038/s41598-020-65840-1>.
- [12] S. Tanaka, Y.V. Kaneti, N.L.W. Septiani, S.X. Dou, Y. Bando, M.S.A. Hossain, J. Kim, Y. Yamauchi, A Review on Iron Oxide-Based Nanoarchitectures for Biomedical, Energy Storage, and Environmental Applications, *Small Methods.* 3 (5) (2019) 1800512, <https://doi.org/10.1002/smt.d.v3.510.1002/smt.d.201800512>.
- [13] M.K. Masud, J. Na, M. Younus, M.S.A. Hossain, Y. Bando, M.J.A. Shiddiky, Y. Yamauchi, Superparamagnetic nanoarchitectures for disease-specific biomarker detection, *Chem. Soc. Rev.* 48 (24) (2019) 5717–5751, <https://doi.org/10.1039/C9CS00174C>.
- [14] A. Ali, H. Zafar, M. Zia, I. ul Haq, A.R. Phull, J.S. Ali, A. Hussain, Synthesis, characterization, applications, and challenges of iron oxide nanoparticles, *Nanotechnol. Sci. Appl.* 9 (2016) 49–67, <https://doi.org/10.2147/NSA.S99986>.
- [15] F. Gao, Q.i. Qi, X. Wu, J. Yu, J. Yao, Z. Cao, Y. Mi, Q. Cui, Multifunctional poly (quaternary ammonium)/Fe₃O₄ composite nanogels for integration of antibacterial and degradable magnetic redox-responsive properties, *Colloids Surfaces A Physicochem. Eng. Asp.* 615 (2021) 126235, <https://doi.org/10.1016/j.colsurfa.2021.126235>.
- [16] F. Gao, X. Wu, D. Wu, J. Yu, J. Yao, Q.i. Qi, Z. Cao, Q. Cui, Y. Mi, Preparation of degradable magnetic temperature- and redox-responsive polymeric/Fe₃O₄ nanocomposite nanogels in inverse miniemulsions for loading and release of 5-fluorouracil, *Colloids Surfaces A Physicochem. Eng. Asp.* 587 (2020) 124363, <https://doi.org/10.1016/j.colsurfa.2019.124363>.
- [17] H. Su, Z. Ye, N. Hmidi, High-performance iron oxide-graphene oxide nanocomposite adsorbents for arsenic removal, *Colloids Surfaces A Physicochem. Eng. Asp.* 522 (2017) 161–172, <https://doi.org/10.1016/j.colsurfa.2017.02.065>.
- [18] Y. Yu, L. Yu, K. Shih, J.P. Chen, Yttrium-doped iron oxide magnetic adsorbent for enhancement in arsenic removal and ease in separation after applications, *J. Colloid Interface Sci.* 521 (2018) 252–260, <https://doi.org/10.1016/j.jcis.2018.02.046>.
- [19] M. Usman, A.I. Belkasm, I.A. Kastoyiannis, M. Ernst, Pre-deposited dynamic membrane adsorber formed of microscale conventional iron oxide-based adsorbents to remove arsenic from water: application study and mathematical modeling, *J. Chem. Technol. Biotechnol.* 96 (6) (2021) 1504–1514, <https://doi.org/10.1002/jctb.6728>.
- [20] S.I. Siddiqui, S.A. Chaudhry, Iron oxide and its modified forms as an adsorbent for arsenic removal: a comprehensive recent advancement, *Process Saf. Environ. Prot.* 111 (2017) 592–626, <https://doi.org/10.1016/j.psep.2017.08.009>.
- [21] H. Wang, X. Zhao, X. Han, Z. Tang, S. Liu, W. Guo, C. Deng, Q. Guo, H. Wang, F. Wu, X. Meng, J.P. Giesy, Effects of monovalent and divalent metal cations on the aggregation and suspension of Fe₃O₄ magnetic nanoparticles in aqueous solution, *Sci. Total Environ.* 586 (2017) 817–826, <https://doi.org/10.1016/j.scitotenv.2017.02.060>.
- [22] C.-H. Liu, Y.-H. Chuang, T.-Y. Chen, Y. Tian, H. Li, M.-K. Wang, W. Zhang, Mechanism of Arsenic Adsorption on Magnetite Nanoparticles from Water: thermodynamic and Spectroscopic Studies, *Environ. Sci. Technol.* 49 (13) (2015) 7726–7734, <https://doi.org/10.1021/acs.est.5b00381>.
- [23] J. Yao, F. Gao, X. Liang, Y. Li, Y. Mi, Q. Qi, J. Yao, Z. Cao, Efficient preparation of carboxyl-functionalized magnetic polymer/Fe₃O₄ nanocomposite particles in one-pot miniemulsion systems, *Colloids Surfaces A Physicochem. Eng. Asp.* 570 (2019) 449–461, <https://doi.org/10.1016/j.colsurfa.2019.03.055>.
- [24] P. Suresh Kumar, T. Prot, L. Korving, K.J. Keesman, I. Dugulan, M.C.M. van Loosdrecht, G.J. Witkamp, Effect of pore size distribution on iron oxide coated granular activated carbons for phosphate adsorption - Importance of mesopores, *Chem. Eng. J.* 326 (2017) 231–239, <https://doi.org/10.1016/j.cej.2017.05.147>.
- [25] S. You, S.W. Ho, T. Li, T. Maneerung, C.H. Wang, Techno-economic analysis of geopolymer production from the coal fly ash with high iron oxide and calcium

- oxide contents, *J. Hazard. Mater.* 361 (2019) 237–244, <https://doi.org/10.1016/j.jhazmat.2018.08.089>.
- [26] S. Sharma, A. Hasan, N. Kumar, L.M. Pandey, Removal of methylene blue dye from aqueous solution using immobilized *Agrobacterium fabrum* biomass along with iron oxide nanoparticles as biosorbent, *Environ. Sci. Pollut. Res.* 25 (22) (2018) 21605–21615, <https://doi.org/10.1007/s11356-018-2280-z>.
- [27] M.H. Zeeshan, R.U. Khan, M. Shafiq, A. Sabir, Polyamide intercalated nanofiltration membrane modified with biofunctionalized core shell composite for efficient removal of Arsenic and Selenium from wastewater, *J. Water Process Eng.* 34 (2020) 101175, <https://doi.org/10.1016/j.jwpe.2020.101175>.
- [28] Z. Du, M. Ji, R. Li, Enhanced membrane fouling control and trace organic compounds removal during microfiltration by coupling coagulation and adsorption in an electric field, *Sci. Total Environ.* 795 (2021) 148830, <https://doi.org/10.1016/j.scitotenv.2021.148830>.
- [29] D. Morillo, G. Pérez, M. Valiente, Efficient arsenic(V) and arsenic(III) removal from acidic solutions with Novel Forager Sponge-loaded superparamagnetic iron oxide nanoparticles, *J. Colloid Interface Sci.* 453 (2015) 132–141, <https://doi.org/10.1016/j.jcis.2015.04.048>.
- [30] A.V. Samrot, H.H. Ali, J. Selvarani, A. E. Faradjeva, R. P. P. S. Kumar S, Adsorption efficiency of chemically synthesized Superparamagnetic Iron Oxide Nanoparticles (SPIONs) on crystal violet dye, *Curr. Res. Green Sustain. Chem.* 4 (2021) 100066, <https://doi.org/10.1016/j.crgsc.2021.100066>.
- [31] L. Simonelli, C. Marini, W. Olszewski, M. Ávila Pérez, N. Ramanan, G. Guilera, V. Cuartero, K. Klementiev, Clæss, The hard X-ray absorption beamline of the ALBA CELLS synchrotron, *Cogent Phys.* 3 (2016) 1231987, <https://doi.org/10.1080/23311940.2016.1231987>.
- [32] B. Ravel, M. Newville, ATHENA, ARTEMIS, HEPHAESTUS: Data analysis for X-ray absorption spectroscopy using IFEFFIT, *J. Synchrotron Radiat.* 12 (4) (2005) 537–541, <https://doi.org/10.1107/S0909049505012719>.
- [33] Y. Xiong, Q. Tong, W. Shan, Z. Xing, Y. Wang, S. Wen, Z. Lou, Arsenic transformation and adsorption by iron hydroxide/manganese dioxide doped straw activated carbon, *Appl. Surf. Sci.* 416 (2017) 618–627, <https://doi.org/10.1016/j.apsusc.2017.04.145>.
- [34] J.O. De Marques Neto, C.R. Bellato, J.L. Milagres, K.D. Pessoa, E.S. De Alvarenga, Preparation and evaluation of chitosan beads immobilized with iron(III) for the removal of As(III) and As(V) from water, *J. Braz. Chem. Soc.* 24 (2013) 121–132, <https://doi.org/10.1590/S0103-50532013000100017>.
- [35] Y. Liu, Y. Xiong, P. Xu, Y.a. Pang, C. Du, Enhancement of Pb (II) adsorption by boron doped ordered mesoporous carbon: Isotherm and kinetics modeling, *Sci. Total Environ.* 708 (2020) 134918, <https://doi.org/10.1016/j.scitotenv.2019.134918>.
- [36] H.N. Tran, S.-J. You, A. Hosseini-Bandegharai, H.-P. Chao, Mistakes and inconsistencies regarding adsorption of contaminants from aqueous solutions: a critical review, *Water Res.* 120 (2017) 88–116, <https://doi.org/10.1016/j.watres.2017.04.014>.
- [37] Y. Tong, P.J. McNamara, B.K. Mayer, Adsorption of organic micropollutants onto biochar: a review of relevant kinetics, mechanisms and equilibrium, *Environ. Sci. Water Res. Technol.* 5 (5) (2019) 821–838, <https://doi.org/10.1039/C8EW00938D>.
- [38] B. Adane, K. Siraj, N. Meka, Kinetic, equilibrium and thermodynamic study of 2-chlorophenol adsorption onto *Ricinus communis* pericarp activated carbon from aqueous solutions, *Green Chem. Lett. Rev.* 8 (3–4) (2015) 1–12, <https://doi.org/10.1080/17518253.2015.1065348>.
- [39] E.C. Lima, A. Hosseini-Bandegharai, J.C. Moreno-Piraján, I. Anastopoulos, A critical review of the estimation of the thermodynamic parameters on adsorption equilibria. Wrong use of equilibrium constant in the Van't Hoff equation for calculation of thermodynamic parameters of adsorption, *J. Mol. Liq.* 273 (2019) 425–434, <https://doi.org/10.1016/j.molliq.2018.10.048>.
- [40] J. Gimenez, M. Martinez, J. Depablo, M. Rovira, L. Duro, Arsenic sorption onto natural hematite, magnetite, and goethite, *J. Hazard. Mater.* 141 (3) (2007) 575–580, <https://doi.org/10.1016/j.jhazmat.2006.07.020>.
- [41] Z. Veličković, G.D. Vuković, A.D. Marinković, M.S. Moldovan, A.A. Perić-Grujić, P.S. Uskoković, M.D. Ristić, Adsorption of arsenate on iron(III) oxide coated ethylenediamine functionalized multiwall carbon nanotubes, *Chem. Eng. J.* 181–182 (2012) 174–181, <https://doi.org/10.1016/j.cej.2011.11.052>.
- [42] B. Moraga, L. Toledo, L. Jelínek, J. Yañez, B.L. Rivas, B.F. Urbano, Copolymer-hydrous zirconium oxide hybrid microspheres for arsenic sorption, *Water Res.* 166 (2019) 115044, <https://doi.org/10.1016/j.watres.2019.115044>.
- [43] A.M.A. Pintor, B.R.C. Vieira, S.C.R. Santos, R.A.R. Boaventura, C.M.S. Botelho, Arsenate and arsenite adsorption onto iron-coated cork granulates, *Sci. Total Environ.* 642 (2018) 1075–1089, <https://doi.org/10.1016/j.scitotenv.2018.06.170>.
- [44] X. Yu, S. Tong, M. Ge, J. Zuo, C. Cao, W. Song, One-step synthesis of magnetic composites of cellulose@iron oxide nanoparticles for arsenic removal, *J. Mater. Chem. A* 1 (3) (2013) 959–965, <https://doi.org/10.1039/C2TA00315E>.
- [45] A. Sigdel, J. Park, H. Kwak, P.K. Park, Arsenic removal from aqueous solutions by adsorption onto hydrous iron oxide-impregnated alginate beads, *J. Ind. Eng. Chem.* 35 (2016) 277–286, <https://doi.org/10.1016/j.jiec.2016.01.005>.
- [46] X. Song, Y. Wang, L. Zhou, X. Luo, J. Liu, Halloysite nanotubes stabilized polyurethane foam carbon coupled with iron oxide for high-efficient and fast treatment of arsenic(III/V) wastewater, *Chem. Eng. Res. Des.* 165 (2021) 298–307, <https://doi.org/10.1016/j.cherd.2020.11.001>.
- [47] R. Amen, H. Bashir, I. Bibi, S.M. Shaheen, N.K. Niazi, M. Shahid, M.M. Hussain, V. Antoniadis, M.B. Shakoob, S.G. Al-Solaimani, H. Wang, J. Bundschuh, J. Rinklebe, A critical review on arsenic removal from water using biochar-based sorbents: The significance of modification and redox reactions, *Chem. Eng. J.* 396 (2020) 125195, <https://doi.org/10.1016/j.cej.2020.125195>.
- [48] Y. Wu, R.K. Kukkadapu, K.J.T. Livi, W. Xu, W. Li, D.L. Sparks, Iron and Arsenic Speciation during As(III) Oxidation by Manganese Oxides in the Presence of Fe (II): Molecular-Level Characterization Using XAFS, Mössbauer, and TEM Analysis, *ACS Earth Sp. Chem.* 2 (3) (2018) 256–268, <https://doi.org/10.1021/acsearthspacechem.7b0011910.1021/acsearthspacechem.7b00119.s001>.
- [49] G. Ona-Nguema, G. Morin, F. Juillot, G. Calas, G.E. Brown, EXAFS Analysis of Arsenite Adsorption onto Two-Line Ferrihydrite, Hematite, Goethite, and Lepidocrocite, *Environ. Sci. Technol.* 39 (23) (2005) 9147–9155, <https://doi.org/10.1021/es050889p10.1021/es050889p.s001>.
- [50] X. Dong, L.Q. Ma, J. Gress, W. Harris, Y. Li, Enhanced Cr(VI) reduction and As(III) oxidation in ice phase: Important role of dissolved organic matter from biochar, *J. Hazard. Mater.* 267 (2014) 62–70, <https://doi.org/10.1016/j.jhazmat.2013.12.027>.
- [51] P. Pędziwiatr, F. Mikołajczyk, D. Zawadzki, K. Mikołajczyk, A. Bedka, Decomposition of hydrogen peroxide - kinetics and review of chosen catalysts, *Acta Innov.* (26) (2018) 45–52, <https://doi.org/10.32933/ActaInnovations10.32933/10.32933/ActaInnovations.2610.32933/ActaInnovations.26.5>.
- [52] B. Chen, Z. Zhu, J. Ma, M. Yang, J. Hong, X. Hu, Y. Qiu, J. Chen, One-pot, solid-phase synthesis of magnetic multiwalled carbon nanotube/iron oxide composites and their application in arsenic removal, *J. Colloid Interface Sci.* 434 (2014) 9–17, <https://doi.org/10.1016/j.jcis.2014.07.046>.
- [53] J.C. Bullen, J.P.L. Kenney, S. Fearn, A. Kafizas, S. Skinner, D.J. Weiss, Improved accuracy in multicomponent surface complexation models using surface-sensitive analytical techniques: adsorption of arsenic onto a TiO₂/Fe₂O₃ multifunctional sorbent, *J. Colloid Interface Sci.* 580 (2020) 834–849, <https://doi.org/10.1016/j.jcis.2020.06.119>.
- [54] J. Alchouron, C. Navarathna, P.M. Rodrigo, H.D. Chludil, A.S. Vega, G. Bosi, F. Perez, D. Mohan, C.U. Pittman Jr., T.E. Mlsna, Household arsenic contaminated water treatment employing iron oxide/bamboo biochar composite: an approach to technology transfer, *J. Colloid Interface Sci.* 587 (2021) 767–779, <https://doi.org/10.1016/j.jcis.2020.11.036>.
- [55] Y. Xu, X. Xie, Y.u. Feng, M.A. Ashraf, YingYing Liu, C. Su, K. Qian, P. Liu, As(III) and As(V) removal mechanisms by Fe-modified biochar characterized using synchrotron-based X-ray absorption spectroscopy and confocal micro-X-ray fluorescence imaging, *Bioresour. Technol.* 304 (2020) 122978, <https://doi.org/10.1016/j.biortech.2020.122978>.